Flexible multifunctional composites with integrated sensing and photo-actuation via hybrid 4D printing

Mei Chen, Ran An, Frédéric Demoly, Hang Jerry Qi, Kun Zhou

Flexible multifunctional composites with integrated sensing and photo-actuation via hybrid 4D printing

Mei Chen, Ran An, Edwin Hang Tong Teo, Frédéric Demoly, H. Jerry Qi, Kun Zhou

M. Chen, R. An, K. Zhou
School of Mechanical and Aerospace Engineering
Nanyang Technological University
Singapore 639798, Singapore
E-mail: kzhou@ntu.edu.sg

E. H. T. Teo
School of Electrical and Electronic Engineering
Nanyang Technological University
Singapore 639798, Singapore

F. Demoly[1,2]
[1]ICB UMR 6303 CNRS
Belfort-Montbeliard University of Technology, UTBM
90010 Belfort, France
[2]Institut universitaire de France
Paris, France

H. J. Qi
The George Woodruff School of Mechanical Engineering
Georgia Institute of Technology
Atlanta, GA 30332, USA

Keyword:

Hybrid 4D printing, multiple smart materials, liquid crystal elastomers, conductive shape memory polymers, integrated sensor-actuator

Abstract:

Four-dimensional (4D) printing, which integrates additive manufacturing with smart materials, facilitates the fabrication of adaptive structures featuring dynamic properties and customizable geometries. The incorporation of multiple smart materials enhances functionalities such as multi-stimuli-responsive actuation and self-sensing. Herein, this work reports a liquid crystal elastomer–shape memory polymer (LCE-SMP) composite through hybrid 4D printing, demonstrating integrated sensing and photo-actuation capabilities. The pioneering multi jet fusion (MJF) 4D printing technique enabled localized and tunable electric conductivity in the SMP, achieved by precisely controlling the dispensing of the carbon black–containing fusing agent. Subsequently, the direct ink writing (DIW) 4D printing of LCE onto the MJF-printed SMP resulted in a multifunctional composite with excellent shape memory, mechanical sensing, photothermal heating, and photothermal actuation. Through the precise control of the structural design and light irradiation, multiple stable temporary configurations under non-stimuli conditions and locally programmable photo-actuation were achieved in a single composite for desirable three-dimensional structure construction and remote object manipulation, including diverse bio- and origami-inspired structures and object locomotion. Simultaneously, self-sensing during corresponding actuations was demonstrated through real-time resistance variations. Beyond applications for desirable actuation, the integrated sensing and photo-actuation capabilities provide real-time monitoring, offering valuable feedback on device performance and operational status. This work introduces a novel concept for designing and fabricating multifunctional material to advance the field of intelligent devices.

1. Introduction

Flexible multifunctional composites can achieve multiple functional tasks, such as sensing, actuation, locomotion, or energy harvesting within a single architecture [1-3]. Such materials hold tremendous promise across diverse fields, including biomedicine, aerospace, soft robotics, wearable electronics, and energy [4-9]. In the advancement of flexible multifunctional composites, it is highly desirable to achieve large, rapid, and reversible actuation with concurrent real-time sensing capabilities, such as action self-sensing and active sensing [10-14]. To enhance environment adaptability in corresponding applications, achieving multi-stable configurations and tunable shape-morphing that can be modulated by various external stimuli is another highly coveted yet challenging attribute.

Smart soft materials, including shape memory polymers (SMPs) [15-17], hydrogels [18-20], and liquid crystal elastomers (LCEs) [21-24], have gained significant research attention for their inherent shape-morphing behavior in response to external stimuli. Among these, one-way SMPs based on phase transition, transitioning from a stable temporary shape to their original shape at the critical temperature, have demonstrated sustained commercial applications, including self-deployable hinges and smart surgery devices [15]. In contrast, LCEs stands out for their unique capacity for large, rapid, reversible, and anisotropic shape changes, making them promising materials in soft robotics, active metamaterials, optics, and textiles [25-29]. Intrinsically, thermal-mechanical responsiveness is the most conventional actuation mode for both SMPs and LCEs. To enhance their functionalities, the corporation of functional dopants into SMP and LCE matrix has been demonstrated, effectively enabling multifunctionality and responsiveness to multiple stimuli [15, 30]. For example, LCEs doped with fillers such as carbon nanotubes (CNTs) [31], carbon black (CB) [32], liquid metal [33-36], Titanium nanocrystals [37], or gold nanoparticles [38-40], exhibit simultaneous responses to heat, electric field, and infrared (IR) light. Similarly, electrically conductive SMPs containing dopants such as CNTs [41], graphene [42], CB [13, 43], or silver nanoparticles [44], can serve as an integrated sensor-actuator with simultaneous sensation and actuation.

On the processing side, 4D printing revolutionizes material processing by integrating smart materials with customizable structural topology enabled by 3D printing [45-47]. Notably, extrusion-based direct ink writing (DIW) is the most utilized

in 4D printing due to its cost-effectiveness, adaptability to diverse materials, and the capability to align fillers or molecules along the printing path. Multi jet fusion (MJF), an emerging multi-material printing technique, combines a multi-agent jetting process with powder bed fusion, demonstrating significant promise in rapidly producing support-free functional polymers with intricate geometries [48]. While recent work showcased the fabrication of shape-adaptive conductive elastomers using MJF [49, 50], the application of MJF in printing smart materials remains a significant area for exploration in 4D printing. Moreover, conventional 4D-printed structures often rely on single smart materials, thereby presenting inherent limitations when utilized alone. For example, while LCE-based structures exhibit reversible and continuous shape changes, the actuated shapes require constant stimulation. Conversely, the deformed configuration of SMP-based structures can remain stable after external stress and stimulus removal, yet these are often restricted to irreversible and discontinuous shape changes.

Recent advances in 4D printing explore the integration of multiple smart materials to create novel multifunctional composites. This involves combining diverse smart materials into single structures through multi-material 4D printing or integrating multiple printing techniques [51-56]. For example, a breakthrough was achieved with hydrogel and SMP composites using multi-material DIW 4D printing, offering diffusion-dependent reversible actuation and highly enhanced bending stiffness [51]. Additionally, hybrid DIW-digital light processing (DLP) 4D printing fabricated of bilayer composite architectures by integrating LCE and SMP, enabling rapid, reversible actuation and cooling-rate mediated tunable shape morphing [52]. Despite these developments, 4D printing multiple smart materials with integrated sensing and actuation capabilities remains unexplored. There is a growing need to develop novel 4D printing techniques and multi-functional composites with customizable geometries for large, rapid, reversible, remotely controllable shape morphing and desirable sensing properties.

In this work, we present the development of a novel bilayer composite comprising a conductive SMP and an LCE with integrated sensing and photo-actuation abilities via hybrid 4D printing (**Figure 1**). By pioneering MJF 4D printing, SMPs with locally controllable conductivity can be rapidly fabricated by precisely tailoring the dispensing of a CB-containing fusing agent (FA) onto a thermoplastic polyurethane (TPU) powder bed (**Figure 1a**). Subsequently, the DIW 4D printing technique was employed to print

LCEs with desirable mesogen alignment onto MJF-printed SMP structures (**Figure 1b**). With precise control of structural design and light irradiation, the resulting 4D-printed LCE-SMP composite demonstrated not only multiple stable temporary configurations under non-stimuli conditions and passive mechanical sensing, but also locally programmable and reprogrammable reversible photo-actuation and self-sensing during corresponding actuations (**Figure 1c**). This work not only introduces a novel 4D printing technique but also presents innovative concepts for the design and fabrication of intelligent devices with multiple functionalities.

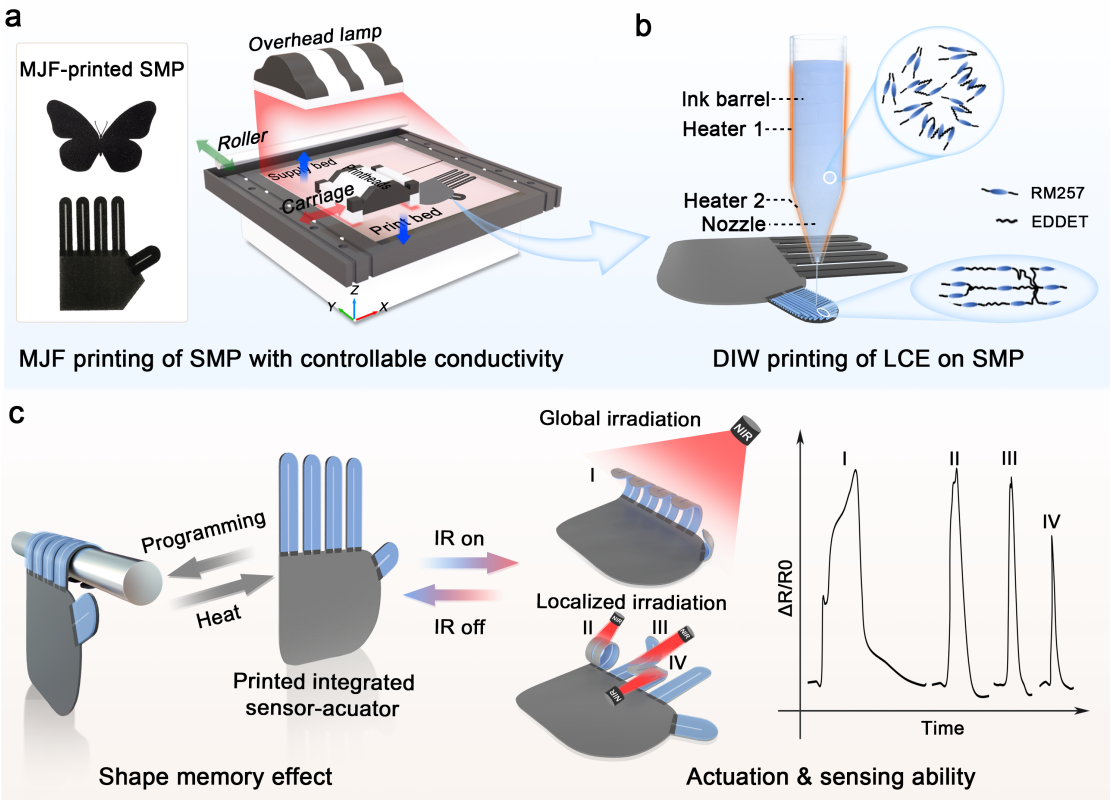

Figure 1. Schematics of 4D-printed LCE-SMP bilayer composite for integrated sensing and photo-actuation. The figure illustrates the hybrid 4D-printing process of the LCE-SMP composite using sequential (a) MJF and (b) DIW 4D printing, and (c) the programmable shape-morphing and self-sensing properties of the printed composite. The colored arrows in 1a represent the movement direction of the corresponding components.

2. Results and discussion

2.1 MJF 4D printing of conductive SMP

While existing research on MJF mainly focused on the mechanical and flame-retardant

properties of printed parts, there is a notable gap in the exploration of other functional properties, such as electrical conductivity. Owing to the intrinsic electrical conductivity, unique temperature resistance, and pressure resistance characteristics of CB particles [13, 57], the commercial CB-containing FA is expected to not only serve as an IR-absorbing colorant that converts the IR light into the thermal energy essential for powder fusion, but also impart printed parts with electrical conductivity. Therefore, this work aims to achieve locally controllable electrical conductivity in MJF-printed SMP parts by site-specifically regulating the commercial FA dispensing amount during the printing process.

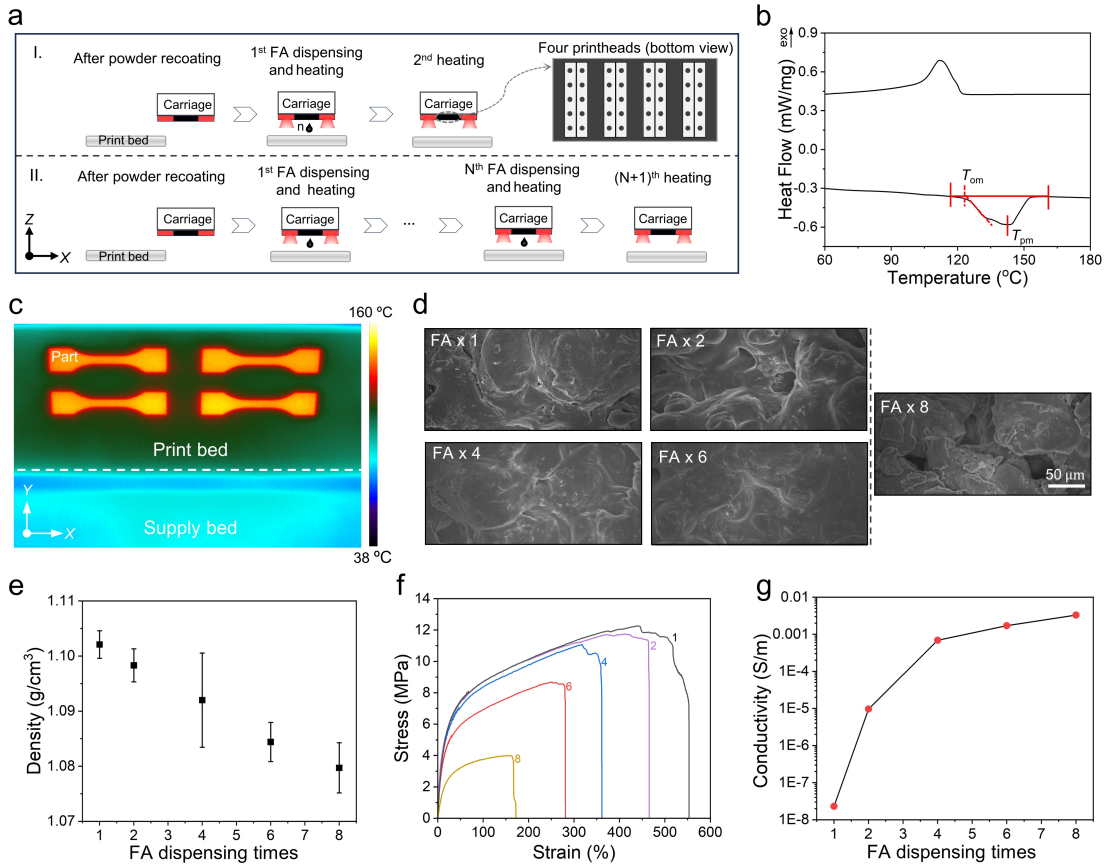

Figure 2. MJF 4D printing of SMPs with controllable mechanical and electrically conductive properties. (a) Precise control over the specific quantity of the dispensed agent per printing layer by tailoring the number of (i) active printheads or (ii) carriage scan passes. (b) DSC curve of SMP powder. (c) Typical temperature profiles recorded by an IR camera during the printing process. (d) SEM images of SMP parts printed with various FA dispensing times. "FA × n" denotes "n" times of FA dispensing. (e) Densities, (f) stress-stain curves, and (g) electrical conductivities of SMP parts printed with FA dispensing times from one to eight.

In a typical MJF printing process, the ink carriage moves side to side above the print bed, dispensing the dark-colored FA in a predetermined pattern on the powder bed

[49, 50]. This FA deposition methodology facilitates the selective fusion of powder particles under global IR irradiation (as shown in **Figure 1a**). By convention, the moving direction of ink carriage was defined as the *X* axis, and the powder recoating direction was defined as the *Y* axis. As illustrated in **Figure 2a**, precise control over the quantity of the dispensed FA per printing layer, denoted by dispensing times, can be achieved by activating multiple printheads (maximum four dispensing times within a single pass, **Figure 2a(i)**) or by employing multiple carriage scan passes (**Figure 2a(ii)**). In this work, the desired dispense times was achieved by using one printhead in multiple scanning passes to ensure adequate powder fusion. The main printing process was detailed in the Experimental Section.

As shown in **Figure 2b**, the DSC curves illustrated that the SMP powder possessed an onset melting temperature T_{om} of 122 °C and a peak melting temperature T_{pm} of 142 °C. To achieve well-fused parts with defined edges the print bed temperature of FA-dispensed regions should be heated to 135-150 °C, while the temperature in regions without FA should be maintained below 120 °C (**Figure 2c**). The optimization of the MJF printing process with varied FA dispensing times focused on achieving high printing efficiency while ensuring the desired fusing temperature (detailed in **Table S1)**. Notably, it was observed that the average fusing temperature could exceed 135 °C with up to six FA dispensing times. However, the maximum fusing temperature of the FA-dispensed region with eight dispensing times only reached 115 °C as the region without FA reached 120 °C, resulting in insufficient powder fusion. With increased heating energy, the surrounding areas without FA exhibited higher temperatures than the FA-dispensed regions, leading to unintended fusion. This phenomenon can be attributed to significant heat loss from solvent evaporation.

The fusion quality of the MJF-printed SMPs with varying FA dispensing times was assessed through the SEM analysis of their microstructures. High-quality fusion was observed in the SMP part printed with up to six dispensing times, where no significant change in the fused microstructure was evident from one to six dispensing times (**Figure 2d**). However, when employing eight dispensing times, visibly unfused powder particles were observed, indicating heightened porosity and a notable decrease in the fusion quality (**Figures 2d&S1**). Furthermore, the densities of the printed SMP parts confirmed that higher FA dispensing times resulted in increased porosity (**Figure**

2e), suggesting a slight decrease in the fusion quality [49]. The effect of dispensing times on the mechanical properties of the MJF-printed SMPs was further investigated. As shown in **Figure 2f** and **Table S2**, an escalation in the dispensing times led to a reduction in the ultimate tensile strength (UTS) and elongation at break, attributed to the increased porosity. Nevertheless, all printed parts exhibited distinct soft elasticity and toughness. Specifically, the UTS decreased from 12.3 MPa (one dispensing time) to 4.0 MPa (eight dispensing times), and the elongation at break declined from 553% (one dispensing time) to 117% (eight dispensing times).

In addition to achieving tunable mechanical properties, effective control over the electrical conductivity of MJF-printed SMPs was realized by tailoring the FA dispensing times, corresponding to the CB particle content. As shown in **Figure 2g**, the conductivity of the printed SMP increased significantly from 2.3×10^{-8} S m^{-1} (one dispensing time) to 3.3×10^{-3} S m^{-1} (eight dispensing times), indicating the transition from insulating to typical electrically conductive ($> 10^{-3}$ S m^{-1}). In accordance with percolation theory [13, 58, 59], a percolation threshold was identified, leading to the establishment of a continuous conductive path as the filler content surpassed the threshold. Thermogravimetric analysis (TGA) further disclosed that the mass fraction of CB particles in an insulating SMP part with one FA dispensing time was approximately 2.44 wt%, whereas in a SMP part demonstrating typical electrical conductivity with six FA dispensing times, it increased to 4.79 wt% (**Figure S2** & **Table S3**).

Moreover, MJF technique not only demonstrated the fabrication of complex structure with homogenous conductivity but also enabled the integrated printing of parts with anisotropic conductivity through site-specific control over FA dispensing (inset of **Figure 1a** and **Figure S3**). This capability offers a cost-effective and assembly-free method for fabricating intricate 3D objects with embedded electrical circuits, presenting significant potential in smart flexible electronics and related fields. To strike a balance between electrical conductivity and mechanical properties, the SMP printed with six dispensing times was identified as the optimal choice for the MJF fabrication of conductive SMP, while the SMP with one dispensing time was employed for the

insulating part in the rest of this wok unless otherwise specified.

2.2 Shape memory property and passive sensing ability of MJF-printed conductive SMP

The thermal properties of amorphous polymers, particularly the glass transition temperature (T_g), play a crucial role in triggering their shape memory behaviors [15]. The DSC curve in **Figure 3a** revealed that the MJF-printed SMP exhibited a T_g of 50 °C and T_{om} of 115 °C, indicating a moderate shape programming temperature and a wide working temperature range. The shape memory properties of the printed SMP were assessed through a shape programming process (**Figure 3b(i)**), as detailed in the Experimental Section. To showcase macroscopic shape memory behavior, a rectangular conductive SMP sheet (40 mm × 15 mm × 0.4 mm) was employed. **Figure 3b(ii)** revealed that the MJF-printed flat sheet can be manually manipulated into various temporary shapes with different curvatures and symmetric or asymmetric structures. Importantly, these deformed shapes can be retained at room temperature without the need for external stimuli. Upon reheating, the deformed sheet reverted to its original flat state, showing excellent shape programmability and re-programmability.

For a quantitative evaluation of the shape memory effect, a shape memory cycle was conducted using a tensile method, and the shape fixity ratio (R_f) and shape recovery ratio (R_r) were calculated (detailed in the Experimental section). The results in **Figure 3c** showed that R_f approached 100% in all cycles, demonstrating the outstanding shape retention ability of MJF-printed SMP. In the initial cycle, R_r was only 74%, reflecting suboptimal recovery attributed to residual stress after printing, a common occurrence in printed SMPs. After several cycles, both the R_f and R_r approached 100%, indicating the exceptional shape memory performance and repeatability of the MJF-printed SMP.

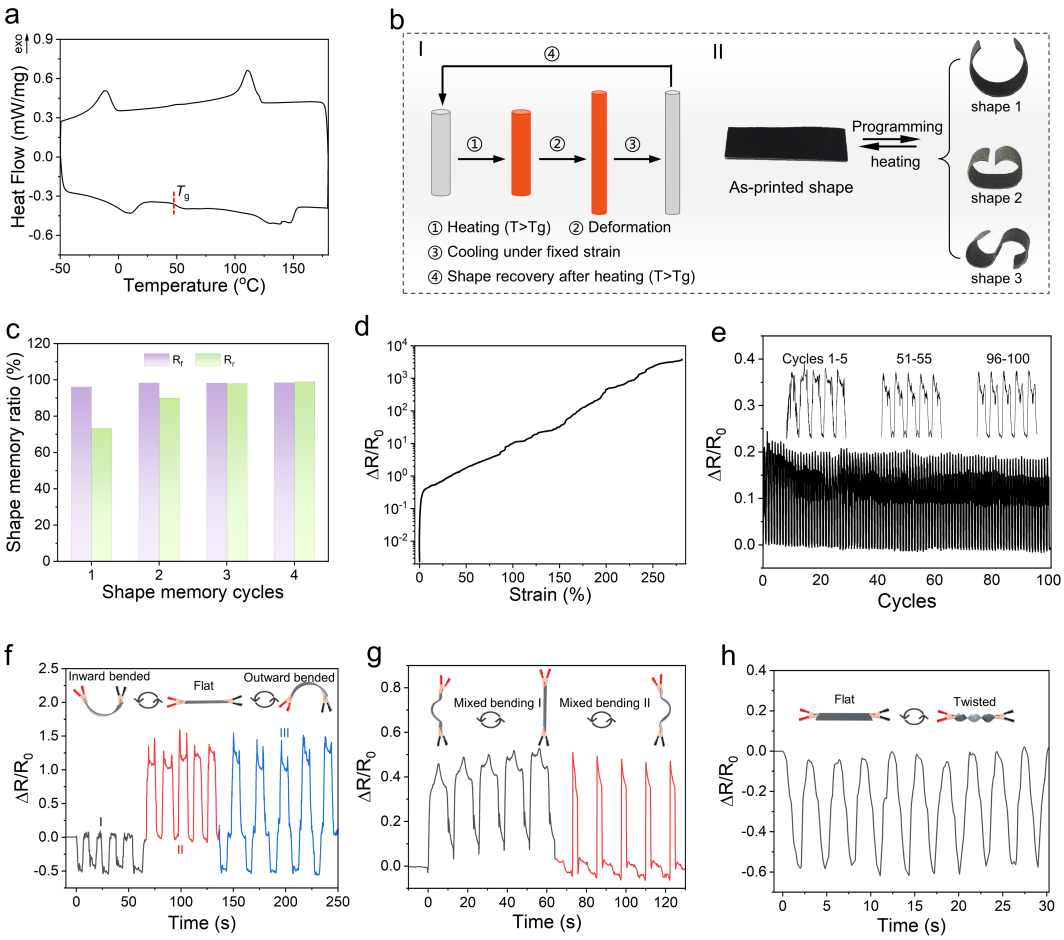

Figure 3. Shape memory performance and sensing properties of the MJF-printed conductive SMP with six FA dispensing times. (a) DSC curve. (b) Schematics of the shape programming process and digital photos of the shape changing behaviors. (c) quantitative shape memory properties. (d) relative resistance versus tensile strain. (e) Cyclic test result for 100 stretching-releasing cycles. The zoomed-in plots in the insets show the stable variation at different testing stages. (f-h) A printed conductive SMP sheet acted as passive strain sensor for sensing various mechanical stimuli.

Similarly to other flexible conductive polymer composites, the MJF-printed conductive SMP holds significant promise as a mechanical stimulus–responsive sensor for applications like wearable devices, owing to its electrical conductivity that changes with structural deformation [13, 15]. In **Figure 3d**, the change in the normalized resistance $\Delta R/R_0$ of the MJF-printed conductive SMP (40 mm × 15 mm × 0.8 mm) during constant stretching is illustrated. Here, ΔR represents the change in resistance at any instance of deformation, and R_0 is the initial resistance. The $\Delta R/R_0$ variation with strain exhibited a gradual increase in the beginning, followed by an exponential rise at a high strain. This behavior corresponds to the nonlinear region in the piezoresistive

response, attributed to an increase in the spacing between conductive fillers. The gauge factor GF, a key sensitivity parameter, was calculated by determining the slope of the plot of $\Delta R/R_0$ against strain. The MJF-printed conductive SMP achieved a GF of 8.2 under a small stain of below 5%. With further stretching, the maximum GF of 5871 at the stain range of 220-280% was achieved, indicating a wide strain detection range and high strain sensitivity (**Figure S4**). Moreover, **Figure 3e** shows a stable variation in the resistance over 100 stretching-releasing cycles with the strain set at 5%, confirming the consistent and stable strain-sensing performance of the MJF-printed conductive SMP.

Beyond simple tensile deformation, the electrical signal response to complex mechanical stimuli, including unidirectional bending, combined bending with multiple directions, and twisting, were thoroughly investigated. Here, "inward bending" refers to bending toward the top surface of the printed part, while "outward bending" refers to bending away from the top surface. As shown in **Figures 3f&S5a**, the MJF-printed conductive SMP exhibited stable and repeatable electrical signals in response to inward bending (I), outward bending (II), and alternative inward-outward bending (III) deformations, demonstrating its excellent bending-direction sensing capabilities. Specifically, inward bending resulted in a decrease in resistance, while outward bending led to an increase in resistance. This directional sensitivity can be attributed to changes in the spacing between CB particles [13, 49, 50]. Outward bending introduces a stretch-like effect, causing larger expansion in the SMP matrix than in the rigid CB particle, resulting in an increase in CB spacing and subsequently an increase in the electrical resistance. Conversely, inward bending compresses the conductive material, decreasing CB spacing and reducing resistance. Furthermore, the printed conductive SMP demonstrated the ability to detect complex structural deformations, such as mixed bending mode (**Figures 3g&S5b**) and twisting (**Figures 3h&S5c**), with a stable and reproducible response. These capabilities position the printed conductive SMP as a promising candidate for monitoring diverse human or machine motions, making it particularly advantageous in fields such as healthcare, flexible robotics, and human-machine interfaces.

2.3 Programmable actuation of LCE-SMP composites printed by hybrid 4D printing

Hybrid 4D printing unlocks the potential for fabricating composites with customizable geometries and versatile functionalities by seamlessly integrating multiple smart materials, facilitating integrated sensing and actuation for advanced applications. Based on this concept, the MJF-printed conductive SMP can be endowed with large, rapid, and reversible actuation capacities by DIW 4D printing LCE onto the MJF-printed SMP substrate (**Figure 1b**). The optimized LCE ink materials and printing processes were established based on our previous research (**Figure S6**) [37]. The strong mesogen alignment of DIW-printed LCE in the printing direction was verified by polarized optical microscopy (POM, **Figures S7a&b**), while a distinctive alignment gradient along the thickness direction was also demonstrated by the reversible bending deformation observed in a single-layer LCE strip, consistent with our prior results (**Figures S7c&d**) [37]. To ensure optimal actuation performance, all LCE-SMP structures feature a two-layer LCE with various printing paths (i.e., mesogen alignment profiles). Notably, the printed LCE-SMP composite exhibited robust interfacial bonding, boasting a high lap shear strength of 2.6 MPa between the LCE and SMP layers with an overlapping area of 10 mm × 0.5 mm (**Figure 4a**). This not only demonstrated the structural integrity but also ensures the seamless realization of synergistic performance from each constituent material.

As expected, the incorporation of LCE imparts programmable thermal actuation to the printed LCE-SMP composite. Simultaneously, the CB-containing SMP enables both remote and local control of photothermal actuation. Prior to exploring photothermal-responsive performance, we evaluated the thermal-mechanical response of the printed LCE-SMP parts. A printed LCE-SMP sheet (40 mm × 15 mm, with an LCE-to-SMP weight ratio of 1) featuring an orthogonal mesogen alignment profile exhibited reversible bending upon heating above the T_{NI} (i.e., the nematic-isotropic transition temperature) (**Figures S8&4b**). Temperature-dependent actuation illustrated an increased bending curvature with increasing temperature **(Figure S9**). Given that the composite underwent fusion when heated beyond the SMP T_{om}, we set 100 °C as the

benchmark actuation temperature for printed LCE-SMP composites. Through controlling both mesogen alignment and specimen geometry, the printed LCE-SMP sheet enabled a variety of reversible thermal-responsive shape-morphing from a 2D flat configuration to diverse 3D shapes, demonstrating its highly programmable thermal-mechanical actuation (**Figure S10**).

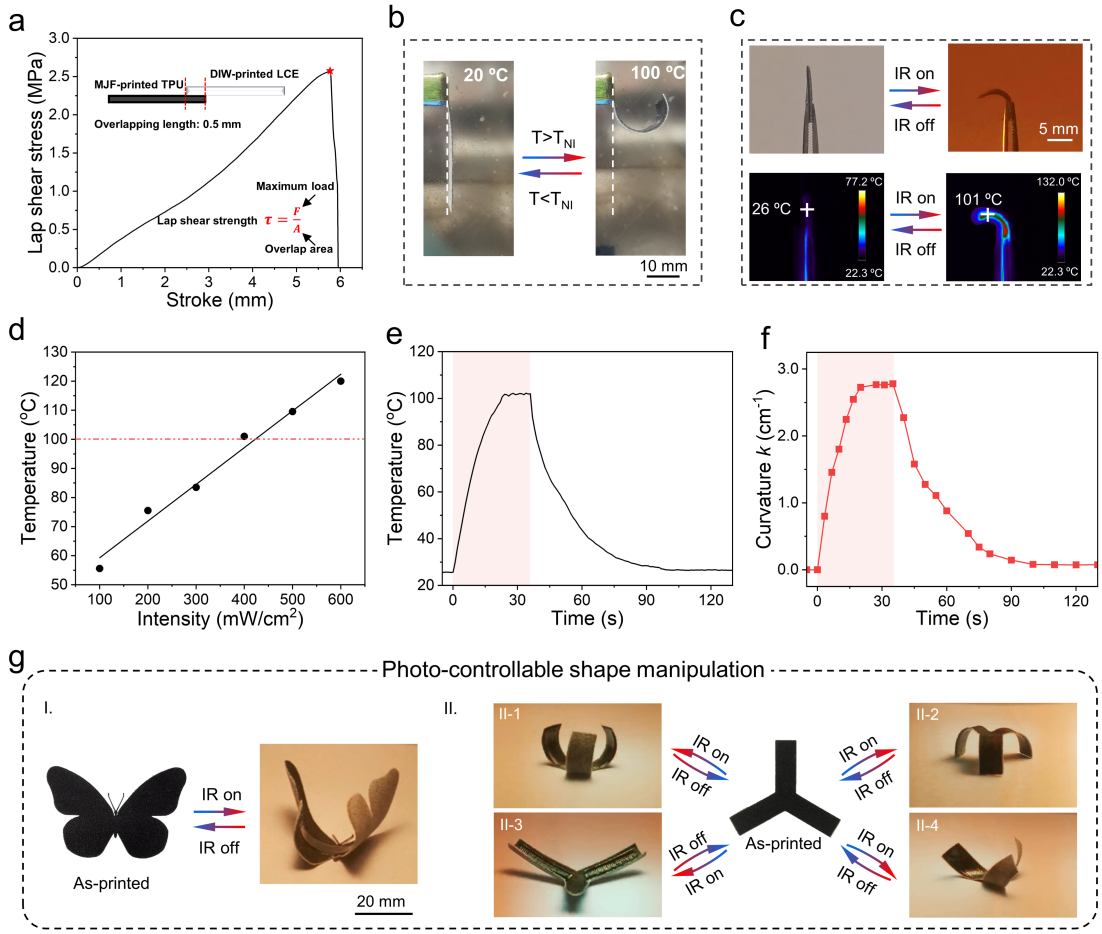

Figure 4. Programmable thermal and photo-responsive behaviors of the 4D-printed LCE-SMP bilayer composites. (a) Lap shear strength between the LCE and SMP layers in the *Z* direction. The insets show the dimensions of the parts and the formula for calculating the lap shear strength, where the overlapping area is 10 mm × 0.5 mm. (b) Digital photos of a printed composite sheet (40 mm by 15 mm, orthogonal alignment) upon heating and cooling. (c) Digital photos and corresponding infrared thermal images showing the shape-bending deformation of a printed composite sheet (10 mm × 10 mm, orthogonal alignment) under NIR irradiation (broadband NIR lamp, 400 mW/cm^2). (d) photothermal heating effects of the bilayer composite sheet under different NIR

intensities. (e) photothermal heating and (f) corresponding bending actuation of the bilayer composite sheet as a function of irradiation time under NIR (400 mW/cm2) irradiation. (g) Digital photos of (i) LCE-SMP butterfly and (ii) LCE-SMP sheet featuring three branches with various stacked structures and mesogen alignment profiles under NIR irradiation.

Leveraging the excellent light-to-heat conversion capability of CB particles, the 4D-printed LCE-SMP composite exhibited remarkable photothermal-mechanical actuation. As shown in **Figure 4c** and **Video S1**, the photo-induced shape-bending behavior of an LCE-SMP sheet (10 mm × 10 mm) under NIR irradiation (broadband NIR lamp, 400 mW/cm^2) was demonstrated, with corresponding infrared thermal images confirming superior photothermal heating. Moreover, we investigated the effect of the NIR intensity on the photothermal behavior of the composite. Significantly, NIR irradiation at 400 mW/cm^2 led to substantial photothermal heating, elevating the temperature of LCE-SMP composite to 100.0 °C (**Figure 4d**). Under this condition, the maximum surface temperature, triggering a maximum curvature k of 2.78 cm^{-1}, was attained in 20 s of NIR irradiation, and promptly reverted to the initial state upon the removal of the NIR light (**Figures 4e&f**). To ensure a rapid and dramatic photo-response, the intensity of the broadband NIR lamp was set at 400 mW/cm^2 throughout the rest of this work unless otherwise specified.

Taking advantage of the reversible photo-responsiveness of LCE-SMP composites and the programmability of 4D printing for both mesogen alignment and 3D geometry, the 4D-printed LCE-SMP composites enable versatile photo-driven 3D structure constructions. For example, **Figures S11(I)&4g(I)** showcase the potential for mimicking butterfly flight, while **Figures S11(II)&4g(II)** demonstrate remarkable flexibility for photo-controllable origami-inspired shape manipulations, including inward bending (II-1), outward bending (II-2), “cigar”-like bending (II-1), “spiral”-like bending (II-3), or twisting (II-4). This programmability in the bending direction upon actuation can be attributed to the gradient alignment effect, as demonstrated in our prior work. Overall, these findings demonstrated the highly programmable photo-responsive

actuation capabilities of the 4D-printed LCE-SMP composite, making it desirable for adaptable soft robotics capable of executing sophisticated tasks via remote control.

2.4 4D-printed LCE-SMP composite for integrated sensor-actuator

The synergetic performance of photo-actuation and self-sensing of the 4D-printed LCE-SMP composite was further demonstrated. In **Figure 5a**, the increase in resistance with the photo-induced temperature elevation of the conductive SMP revealed positive temperature coefficient resistance characteristics of the CB-containing SMP and LCE-SMP composite [13]. The structural design of the LCE-SMP composite sheet, as shown in **Figure S12**, highlighted its ability to undergo diverse shape morphing between 2D flat to 3D configurations, accompanied by real-time changes in electrical signals induced by corresponding photo-actuation (**Figures 5b-d**). The distinct shapes and intensities of output signals exhibit significant variability among different actuations.

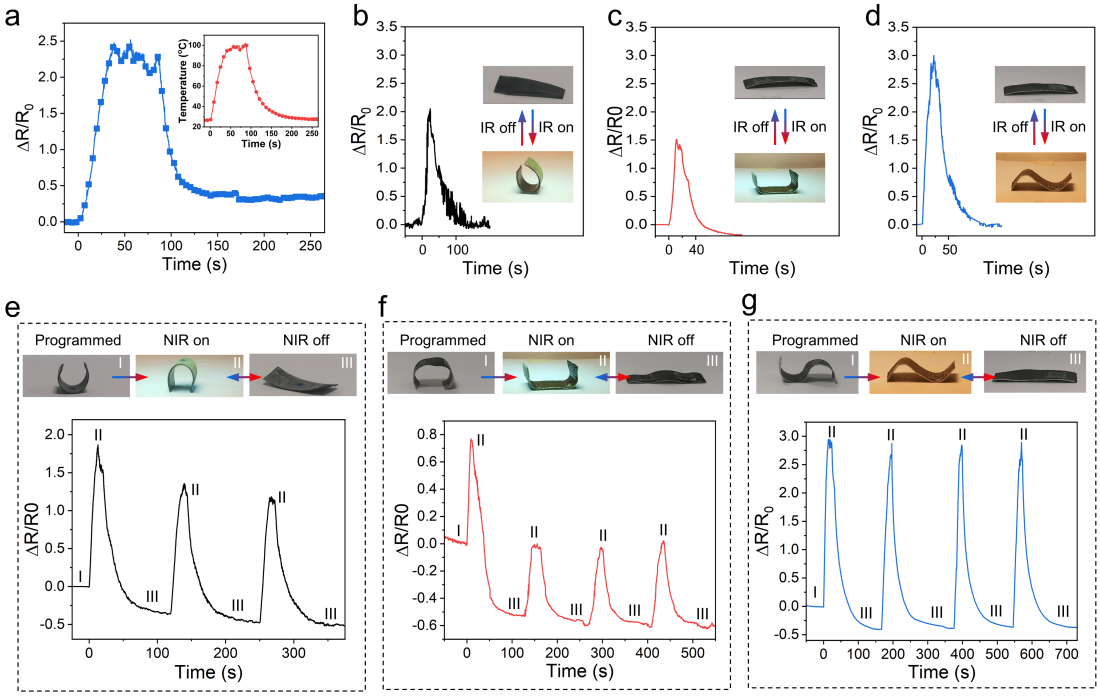

Figure 5. Integrated sensing and photo-actuation properties of 4D-printed LCE-SMP composites. (a) relative resistance variation of a printed SMP sheet as a function of irradiation time under NIR irradiation (broadband lamp, 400 mW/cm^2) (insert: the corresponding photothermal heating). (b-d) The real-time record of the resistance of the LCE-SMP sheets upon NIR irradiation (broadband lamp, 400 mW/cm^2) (insert: the corresponding photothermal shape-morphing images between as-printed flat state and

actuated state). (e-f) The real-time record of the resistance of the pre-programmed LCE-SMP sheets upon repeated NIR irradiation (broadband lamp, 400 mW/cm^2) (insert: the corresponding photothermal shape-morphing images among programmed state (I), actuated state (II) and as-printed flat state (III)).

Through a shape programming process, the initial state of the 4D-printed LCE-SMP sheet can be programmed into diverse deformed temporary shapes. Under NIR irradiation, the printed LCE-SMP sheet transformed from the programmed temporary shape (State I) to the mesogen alignment-dependent actuated shape (State II), and subsequently returned to the initial flat shape (State III) upon NIR removal (**Figures 5e-g**). With repeated NIR irradiation and removal, the composite underwent reversible shape changes between State II and State III. These shape changes can be monitored by analyzing the distinct signals in intensities and the resistance difference between State I and State II. Signal reproducibility analysis underscores the repeatability of the LCE-SMP composite in both actuation and sensing aspects. This integrated sensing and photo-actuation capability not only finds applications in soft robots for tasks like gripping, load-bearing, and intelligent 3D structure construction but also enables real-time monitoring of these actions, providing real-time feedback on device performance and operational status.

In accordance with the electronic tunneling effect theory [13, 49, 58, 59], changes in the resistance of the printed LCE-SMP composite can be attributed to the changes in the spacings between conductive CB nanoparticles induced by photothermal-mechanical stimuli. Upon NIR irradiation, the spacing was determined by two phenomena: (1) the photothermal effect causing volume expansion of the polymer matrix, leading to increased spacing between CB particles; (2) actuation-induced deformation of the polymer matrix, either stretching-like or compression-like, resulting in a corresponding increase or decrease in the spacing between CB particles.

Furthermore, an LCE-SMP composite that can function as a versatile sensor-actuator unit was designed and printed to mimic intelligent biomimetic system. **Figure 6a** illustrates that the MJF-printed SMP features a conductive path printed with six FA

dispensing times and an insulating section printed with one FA dispensing time, while a two-layer LCE with orthogonal alignment profile was then DIW printed onto the conductive path. Notably, the LCE layer can also serve as an insulating encapsulation layer for the conductive SMP.

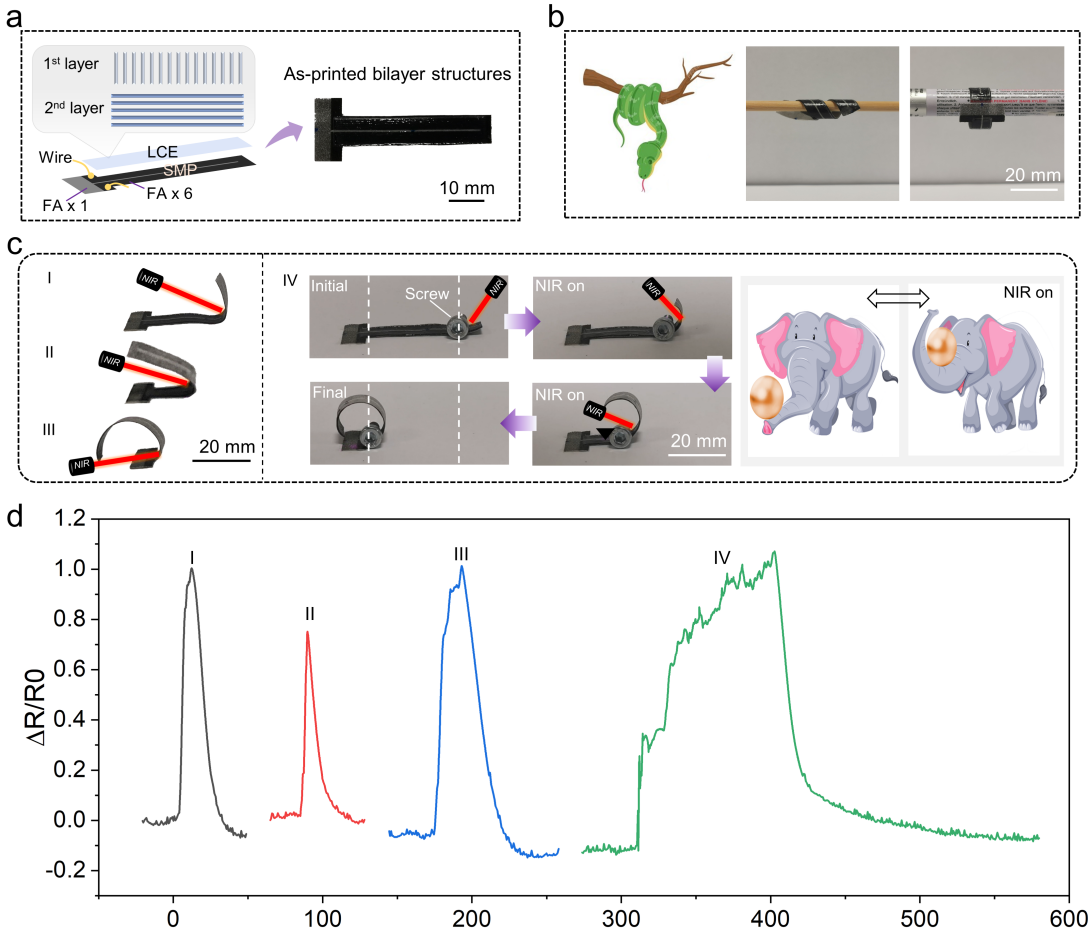

Figure 6. Design and characterization of an assembly-free multifunctional LCE-SMP composite via hybrid 4D printing. (a) Schematic of the LCE-SMP composite consisting of a SMP layer with anisotropic conductivity and a LCE layer with orthogonal mesogen alignment onto the conductive SMP surface. (b) Digital photos of the printed single composite programmed into different temporary shapes adaptively wing around branches with tunable sizes. (c) Digital photos of the locally reprogrammable photo-actuation of the printed single composite via site-specific NIR laser irradiation, including 90° bending (I), 180° bending (II), curling (III), and sequential curling driven weight's forward locomotion (IV). (d) The real-time record of the resistance of the LCE-SMP composite during corresponding photo-actuations.

Benefiting from the shape memory effect, the integrated sensor-actuator can adaptively wind around branches with tunable sizes, resembling a snake for camouflage (**Figure 6b**). Upon NIR irradiation, it can revert from the temporary shape to the initial flat shape. Using an 808 nm NIR laser as the light source, precise control of light exposure enables locally reprogrammable shape-morphing, akin to the site-specific bending and curling movements in a human finger (**Figures 6c(I-III)**). The high output power exerted by the photo-actuation makes it possible to manipulate objects through remote photo-driven means. As demonstrated in **Figure 6c(IV) and Video S2**, precise control of NIR laser irradiation allows the printed composite (0.05 g) to undergo curling movements, propelling the locomotion of a much heavier metal screw (2.00 g). This is equivalent to an elephant's trunk rolling up a trunk with ease. Meanwhile, the corresponding change in the normalized resistance of the composite in **Figure 6d** demonstrated the self-sensing for the photo-driven actuations. Overall, the combination of multiple smart material system and 4D printing technology offers expanded design freedom and possibilities for the application of assembly-free intelligent devices in the future.

3. Conclusion

In this study, we present a novel multifunctional smart composite consisting of LCE and conductive SMP through hybrid 4D printing. Notably, we employed the MJF technique for the first time in 4D printing, achieving tunable electrical conductivity in SMP by precisely controlling the dispensing amount of CB-containing FA. Results demonstrated that MJF-printed conductive SMP exhibited good soft elasticity, excellent shape memory effect, and passive mechanical sensing ability. By combing LCE and SMP into a single composite, their unique thermomechanical properties could be harnessed to generate a composite with programmable temporary shapes, stable without the requirement of constant stimuli, and with the capability for rapid, large, and reversible photothermal shape-morphing. Through the precise control of the structural design and light irradiation, we further achieved the LCE-SMP composite with

customizable geometries and anisotropic conductivity, which not only demonstrated locally reprogrammable photo-actuation for various 3D structure construction and object manipulation, but also enabled self-sensing during corresponding actuations. The multifunctionalities of these soft materials hold immense potential in intelligent systems, especially smart flexible electronics and soft robotics, where a single structure can accomplish multiple tasks simultaneously. This work provides novel insights into the design and preparation of multifunctional composite materials in intelligent devices for advanced applications.

4. Experimental Section

Materials: The MJF-printed SMP utilized in this study was fabricated with a thermoplastic polyurethane (TPU) powder (Ultrasint TPU01, HP Inc., USA) and a commercial CB-contained FA (HP Inc., USA). The CB particles in the FA had an irregular shape with an average size below 20 nm (Figure S13a), and the SMP powder exhibited a broad particle size range of 20-250 μm (Figure S13b).

The LCE employed in this study was DIW 3D printed and prepared in accordance with our previous work. First, the reactive mesogen 1,4-Bis-[4-(3-acryloyloxypropyloxy) benzoyloxy]-2-methylbenzene (RM257) (Sigma-Aldrich Co.) and the chain extender 2,2′-(ethylenedioxy)diethanethiol (EDDET) (Sigma-Aldrich Co.) were dissolved in CH_2Cl_2 (Sigma-Aldrich Co.) at a 1.15:1 ratio. Subsequently, a solution containing 0.2 wt% of the radical inhibitor BHT (Shanghai Aladdin Biochemical Technology Co., Ltd.) and 0.9 wt% of the catalyst TEA (Shanghai Macklin Biochemical Co., Ltd.) in CH_2Cl_2 was added to the mixture, which was stirred on a magnetic mixer at room temperature overnight. Following this, 0.4 wt% of the photo-initiator Irgacure 651 (Sigma-Aldrich Co.) was introduced into the solution. The mixture was stored in an 80 °C oven for 24 hours to ensure complete solvent evaporation. The resulting LCE oligomer ink was loaded into a printing syringe, and the syringe was subjected to a vacuum oven at 80 °C for 4 hours to eliminate any remaining bubbles. To prevent ambient light from curing the oligomer ink, all ink-preparation procedures were carried out under light-blocking conditions.

***MJF 4D printing*:** The SMP printing process was carried out on an MJF testbed with the commercial FA (HP Inc., USA). Delicate adjustments were made to several printing parameters, including the inkjet settings, energy input, temperature of the print bed,

layer thickness, recoating speed, and supply ratio of the powder, to attain an optimal fusing quality and precise dimensions of the printed parts.

The heating system of the testbed comprised an overhead lamp situated above the powder bed and fusing lamps on both sides of the moving carriage. The carriage, capable of accommodating four ink cartridges, each equipped with one printhead containing FA, allowed simultaneous inkjet printing four times at the same location on the powder bed within a single pass. The printhead featured 10,560 nozzles with a diameter of 16 μm, generating 12-pL droplets at a high ejection frequency of 9.6 kHz. Following the recommendation for MJF commercial printing, the percentage of nozzles used for each printhead in each printing job is set to 40%. The carriage scan speed was set at 406 mm s^{-1} with a building layer thickness of 80 μm and a roller speed of 250 mm s^{-1}. The supply ratio, indicating the ratio between the distance of the rising supply bed and that of the descending print bed, was fixed at 1.8 to achieve a dense powder layer. By adjusting the power of the overhead lamp, fusing lamps, and the temperature control system around the print bed, the selected powder region was heated to 130–150 °C to fuse SMP powder particles after FA application. The final parts were constructed layer-by-layer, collected, and subjected to bead blasting for cleaning after printing.

DIW 4D printing*:* The syringe containing the LCE ink was loaded into a DIW 3D printer (Cellink, BIO X), with a maximum pressure of 200 kPa) and preheated to the printing temperature for 20 min. Pressure was applied to the syringe to extrude the material through the ink-deposition nozzle, and the printing path was controlled by the G-code generated from the printer software. The printing parameters were optimized to enable the extrusion process within 200 kPa and to achieve mesogen alignment. Typically, the LCE ink was printed onto a MJF-printed SMP sheet at a syringe temperature of 55 °C (controlled by the built-in 'Heater 1' in **Figure 1b**), nozzle temperature of 45 °C (controlled by "Heater 2" in Figure 1b), nozzle diameter of 410 μm, extrusion pressure of 190 kPa, and printing speed of 1.5 mm s^{-1}. A built-in UV LED (20 mW/cm^2, 365 nm) was used to partially cure the extruded ink during printing. Afterwards, the as-printed structures were fully cured under an external UV lamp (100 mW/cm^2, 365 nm) for 30 min.

Characterization of LCE ink, SMP powder, and CB particles: A differential scanning calorimetry (DSC) test was conducted using a differential scanning calorimeter (DSC-Q200, TA Instruments) with a ramp rate of 10 °C min^{-1} to measure the phase transition temperature of the LCE ink and SMP powder. The rheological properties of the LCE

ink and FA were measured using a rotational rheometer (DHR-2, TA Instruments) at a shear rate ramp from 0.01 to 100 s^{-1}. A 25 mm parallel plate geometry was used, and all inks were tested at their respective printing temperatures. Transmission electron microscope (TEM) measurements were conducted on a JEOL 2010HR microscope at 200 kV to observe the morphology of the CB particles, which were obtained by centrifuging the FA for three times followed by drying.

***Characterization of printed parts*:** The surface morphologies of the MJF-printed SMP were observed by scanning electron microscope (JSM-5600 LV, JEOL, Japan). The densities of the SMP parts were measured by an analytical balance (XS204, Mettler Toledo, USA). The tensile properties of the MJF-printed SMP (40 mm × 15 mm, five building layers) were evaluated by a universal tester (AGX 10 kN, Shimadzu Corp., Japan) at a test speed of 10 mm min^{-1}. Three samples were tested for each group. The lap shear test of the LCE-SMP composite (40 mm × 10 mm) was also conducted by the universal tester at the same speed. The length of the overlapping area was set at 0.5 mm because the samples with an overlapping length larger than that would be unable to separate at the interface.

The thermal properties of the printed conductive SMP part with six FA dispensing times were analyzed by the DSC-Q200 system with a ramp rate of 10 °C min^{-1}. The mass fractions of fillers in the printed conductive SMP were measured by a TGA instrument (TGA-Q500, TA Instruments, USA) with a ramp rate of 10 °C min^{-1} under a nitrogen atmosphere. The molecular alignment of the printed LCE was observed using optical microscopy (VHX-7100, Keyence) equipped with two polarizing films.

The shape memory program for both printed SMP and LCE-SMP composite was processed by first placing the structure in an oven at 75 °C with fixed deformation for 30 min and then placing the structure in a fridge at 0 °C for 30 min to obtain a predesigned temporary shape. The shape memory cycle was conducted on the MJF-printed conductive SMP sheet (40 mm by 15 mm, 5 building layers) to quantitatively evaluate the shape memory effect using a universal tester (AGX 10 kN, Shimadzu Corp., Japan). The procedures were as follows: (i) The rectangular film was thermally equilibrated at 75 °C for 5 min to obtain the initial strain ($\varepsilon_{initial}$) of the N^{th} cycle. Then it was stretched isothermally to 60 N to record the deformed strain (ε_{deform}). (ii) The sample was naturally cooled and kept isothermal at 25 °C for 5 min. (iii) The external force was unloaded and the specimen was equilibrated at 25 °C for 5 min to obtain the fixed strain (ε_{fix}). (iv) The sample was reheated and equilibrated at 75 °C for 10 min. The obtained strain was recorded as the residual strain after recovery ($\varepsilon_{recover}$). Thus, the

shape fixity ratio (R_f) and the shape recovery ratio (R_r) were calculated as follows:

$$R_f(\%) = \frac{\varepsilon_{fix}}{\varepsilon_{deform}} \times 100\% \quad (1)$$

$$R_r(\%) = \frac{\varepsilon_{deform} - \varepsilon_{recover}}{\varepsilon_{deform} - \varepsilon_{initial}} \times 100\% \quad (2)$$

The four-probe conductivity meter (HPS2662, HELPASS, China) was used to test the conductivity of printed SMP parts. The resistance variations of printed SMP parts during various passive mechanical stimuli were tested by a source meter (Keithley 2450, Tektronix Inc., USA) with a source voltage of 10 V. The piezoresistive properties of the printed SMP parts were characterized under stretching until the parts were broken. The tensile test with constant loading was conducted at a test speed of 10 mm min^{-1}. The piezoresistive property of the conductive SMP part (10 mm × 8 mm × 1 mm) under cyclic loading was evaluated in a strain range from 0% to 5% and a test speed of 60 mm min^{-1}. In all resistance tests, two small strips of copper foils were stuck on the parts by silver adhesive (CW2460, Chemtronics, USA), and each was gripped by an alligator clip connected to the source meter.

To study the thermo-actuation response, LCE-SMP samples (40 mm × 10 mm, SMP with 5 building layers and LCE with uniaxial alignment) were fixed at the upper end and placed inside a LabTech oven with an optical access. The samples were heated at a rate of 1 °C/min and were held at each testing temperature for 10 min to ensure full equilibration. Actuation images were captured using a Huawei P30 Pro smartphone, and the deformation curvatures were calibrated and measured using ImageJ software.

Photothermal effects were studied by measuring the surface temperature and bending curvature of the LCE-SMP samples (10 mm × 10 mm, SMP with 5 building layers and LCE with orthogonal alignment) under the irradiation of a broadband NIR lamp using an infrared thermal camera (FLIR Systems) and a Huawei P30 Pro smartphone. Photo-driven actuations were achieved by exposing the LCE-SMP samples into broadband NIR or 808 nm NIR laser light and were recorded using a Huawei P30 Pro smartphone. Meanwhile, the corresponding resistance variations during the photo-actuations were tested by a source meter (Keithley 2450, Tektronix Inc., USA) with a source voltage of 10 V.

References

1. McEvoy, M.A. and N. Correll, *Materials that couple sensing, actuation, computation, and communication.* Science, 2015. **347**(6228): p. 1261689.
2. Narayana, K.J. and R.G. Burela, *A review of recent research on multifunctional composite materials and structures with their applications.* Materials Today: Proceedings, 2018. **5**(2): p. 5580-5590.
3. Lendlein, A. and R.S. Trask, *Multifunctional materials: concepts, function-structure relationships, knowledge-based design, translational materials research.* Multifunctional Materials, 2018. **1**(1): p. 010201.
4. Adam, T.J., et al., *Multifunctional composites for future energy storage in aerospace structures.* Energies, 2018. **11**(2): p. 335.
5. Cho, W., et al., *Multi-functional locomotion of collectively assembled shape-reconfigurable electronics.* Nano Energy, 2023. **118**: p. 108953.
6. Chen, Y., et al., *How far for the electronic skin: from multifunctional material to advanced applications.* Advanced Materials Technologies, 2023. **8**(8): p. 2201352.
7. Qu, C.C., et al., *Flexible wearables for plants.* Small, 2021. **17**(50): p. 2104482.
8. Su, Y., et al., *A wireless energy transmission enabled wearable active acetone biosensor for non-invasive prediabetes diagnosis.* Nano Energy, 2020. **74**: p. 104941.
9. Shklyaev, O.E. and A.C. Balazs, *Interlinking spatial dimensions and kinetic processes in dissipative materials to create synthetic systems with lifelike functionality.* Nature Nanotechnology, 2024. **19**(2): p. 146-159.
10. Qian, C., et al., *A stretchable and conductive design based on multi-responsive hydrogel for self-sensing actuators.* Chemical Engineering Journal, 2023. **454**: p. 140263.
11. Guo, H., et al., *Microsphere Structure Composite Phase Change Material with Anti-Leakage, Self-Sensing, and Photothermal Conversion Properties for Thermal Energy Harvesting and Multi-Functional Sensor.* Advanced Functional Materials, 2023. **33**(1): p. 2209345.
12. Johnson, B., et al., *A multifunctional soft robotic shape display with high-speed actuation, sensing, and control.* Nature Communications, 2023. **14**(1): p. 4516.
13. Chen, D., et al., *4D printing strain self-sensing and temperature self-sensing integrated sensor–actuator with bioinspired gradient gaps.* Advanced Science, 2020. **7**(13): p. 2000584.
14. Cao, X., et al., *Piezoelectric nanogenerators derived self-powered sensors for multifunctional applications and artificial intelligence.* Advanced Functional Materials, 2021. **31**(33): p. 2102983.
15. Xia, Y., et al., *A review of shape memory polymers and composites: mechanisms, materials, and applications.* Advanced materials, 2021. **33**(6): p. 2000713.
16. Ze, Q., et al., *Magnetic shape memory polymers with integrated multifunctional shape manipulation.* Advanced Materials, 2020. **32**(4): p. 1906657.
17. Ni, C., et al., *Shape memory polymer with programmable recovery onset.* Nature, 2023. **622**(7984): p. 748-753.
18. Liu, X., et al., *Recent advances in stimuli-responsive shape-morphing hydrogels.* Advanced Functional Materials, 2022. **32**(39): p. 2203323.
19. Ma, S., et al., *Highly Stretchable and Conductive MXene-Encapsulated Liquid Metal Hydrogels for Bioinspired Self-Sensing Soft Actuators.* Advanced Functional Materials, 2024. **34**(7): p. 2309899.

20. Zhou, T., et al., *3D printable high-performance conducting polymer hydrogel for all-hydrogel bioelectronic interfaces.* Nature Materials, 2023. **22**(7): p. 895-902.
21. Hebner, T.S., et al., *Leaping liquid crystal elastomers.* Science Advances, 2023. **9**(3): p. eade1320.
22. Song, C., et al., *Light-Responsive Programmable Shape-Memory Soft Actuator Based on Liquid Crystalline Polymer/Polyurethane Network.* Advanced Functional Materials, 2023. **33**(17): p. 2213771.
23. Choi, S.H., et al., *Phase patterning of liquid crystal elastomers by laser-induced dynamic crosslinking.* Nature Materials, 2024: p. 1-10.
24. Yao, Y., et al., *Enabling liquid crystal elastomers with tunable actuation temperature.* Nature Communications, 2023. **14**(1): p. 3518.
25. Zhou, X., et al., *Multimodal Autonomous Locomotion of Liquid Crystal Elastomer Soft Robot.* Advanced Science, 2024: p. 2402358.
26. Wang, Q., et al., *Programmable spatial deformation by controllable off-center freestanding 4D printing of continuous fiber reinforced liquid crystal elastomer composites.* Nature Communications, 2023. **14**(1): p. 3869.
27. Wu, J., et al., *Liquid crystal elastomer metamaterials with giant biaxial thermal shrinkage for enhancing skin regeneration.* Advanced Materials, 2021. **33**(45): p. 2106175.
28. Kim, S.-U., et al., *Broadband and pixelated camouflage in inflating chiral nematic liquid crystalline elastomers.* Nature materials, 2022. **21**(1): p. 41-46.
29. Silva, P.E., et al., *Active textile fabrics from weaving liquid crystalline elastomer filaments.* Advanced Materials, 2023. **35**(14): p. 2210689.
30. Wang, Y., J. Liu, and S. Yang, *Multi-functional liquid crystal elastomer composites.* Applied Physics Reviews, 2022. **9**(1).
31. Liu, J., et al., *Shaping and locomotion of soft robots using filament actuators made from liquid crystal elastomer–carbon nanotube composites.* Advanced Intelligent Systems, 2020. **2**(6): p. 1900163.
32. Nie, Z.Z., et al., *Multimodal Self-sustainable Autonomous Locomotions of Light-driven Seifert Ribbon Actuators based on Liquid Crystal Elastomers.* Angewandte Chemie International Edition, 2023. **62**(25): p. e202304081.
33. Maurin, V., et al., *Liquid Crystal Elastomer–Liquid Metal Composite: Ultrafast, Untethered, and Programmable Actuation by Induction Heating.* Advanced Materials, 2023: p. 2302765.
34. Ford, M.J., et al., *A multifunctional shape-morphing elastomer with liquid metal inclusions.* Proceedings of the National Academy of Sciences, 2019. **116**(43): p. 21438-21444.
35. Ambulo, C.P., et al., *4D-Printable liquid metal–liquid crystal elastomer composites.* ACS applied materials & interfaces, 2020. **13**(11): p. 12805-12813.
36. Kotikian, A., et al., *Innervated, self-sensing liquid crystal elastomer actuators with closed loop control.* Advanced Materials, 2021. **33**(27): p. 2101814.
37. Chen, M., et al., *4D printing of reprogrammable liquid crystal elastomers with synergistic photochromism and photoactuation.* Advanced Materials, 2023: p. 2303969.
38. Wang, Y., et al., *Repeatable and reprogrammable shape morphing from photoresponsive gold nanorod/liquid crystal elastomers.* Advanced Materials, 2020. **32**(46): p. 2004270.
39. Skillin, N.P., et al., *Photothermal Actuation of Thick 3D-Printed Liquid Crystalline Elastomer Nanocomposites.* Advanced Materials, 2024: p. 2313745.

40. Sun, Y., et al., *A 3D-Printed Ferromagnetic Liquid Crystal Elastomer with Programmed Dual-Anisotropy and Multi-Responsiveness.* Advanced Materials, 2023. **35**(45): p. 2302824.
41. Cortés, A., et al., *DLP 4D-printing of remotely, modularly, and selectively controllable shape memory polymer nanocomposites embedding carbon nanotubes.* Advanced Functional Materials, 2021. **31**(50): p. 2106774.
42. Wang, Y.C., et al., *Graphene implanted shape memory polymers with dielectric gene dominated highly efficient microwave drive.* Advanced Functional Materials, 2023. **33**(40): p. 2303560.
43. Kong, D., et al., *High temperature electromagnetic shielding shape memory polymer composite.* Chemical Engineering Journal, 2021. **408**: p. 127365.
44. Toncheva, A., et al., *Fast IR-actuated shape-memory polymers using in situ silver nanoparticle-grafted cellulose nanocrystals.* ACS applied materials & interfaces, 2018. **10**(35): p. 29933-29942.
45. Kuang, X., et al., *Advances in 4D printing: materials and applications.* Advanced Functional Materials, 2019. **29**(2): p. 1805290.
46. Chen, M., et al., *Recent advances in 4D printing of liquid crystal elastomers.* Advanced Materials, 2023. **35**(23): p. 2209566.
47. Wan, X., et al., *Recent Advances in 4D Printing of Advanced Materials and Structures for Functional Applications.* Advanced Materials, 2024: p. 2312263.
48. Chen, J., et al., *3D-Printed anisotropic polymer materials for functional applications.* Advanced Materials, 2022. **34**(5): p. 2102877.
49. Chen, J., L. Zhao, and K. Zhou, *Multi-Jet Fusion 3D Voxel Printing of Conductive Elastomers.* Advanced Materials, 2022. **34**(47): p. 2205909.
50. Hou, Y., et al., *3D printed conformal strain and humidity sensors for human motion prediction and health monitoring via machine learning.* Advanced Science, 2023. **10**(36): p. 2304132.
51. Yuan, C., F. Wang, and Q. Ge, *Multimaterial direct 4D printing of high stiffness structures with large bending curvature.* Extreme Mechanics Letters, 2021. **42**: p. 101122.
52. Roach, D.J., et al., *4D Printed Multifunctional Composites With Cooling-Rate Mediated Tunable Shape Morphing.* Advanced Functional Materials, 2022. **32**(36): p. 2203236.
53. Peng, X., et al., *4D printing of freestanding liquid crystal elastomers via hybrid additive manufacturing.* Advanced Materials, 2022. **34**(39): p. 2204890.
54. Peng, X., et al., *Integrating digital light processing with direct ink writing for hybrid 3D printing of functional structures and devices.* Additive Manufacturing, 2021. **40**: p. 101911.
55. Rafiee, M., R.D. Farahani, and D. Therriault, *Multi-material 3D and 4D printing: a survey.* Advanced Science, 2020. **7**(12): p. 1902307.
56. Boley, J.W., et al., *Shape-shifting structured lattices via multimaterial 4D printing.* Proceedings of the National Academy of Sciences, 2019. **116**(42): p. 20856-20862.
57. Lonergan, M.C., et al., *Array-based vapor sensing using chemically sensitive, carbon black–polymer resistors.* Chemistry of Materials, 1996. **8**(9): p. 2298-2312.
58. Sheng, P., *Fluctuation-induced tunneling conduction in disordered materials.* Physical Review B, 1980. **21**(6): p. 2180.
59. Sichel, E.K., J.I. Gittleman, and P. Sheng, *Transport properties of the composite material carbon-poly (vinyl chloride).* Physical Review B, 1978. **18**(10): p. 5712.